www.springer.com/41230
https://doi.org/10.1007/s41230-026-5208-0

Effects of natural and forced convections on dendritic growth in thin-walled Al-Cu alloy by counter-gravity casting: A phase-field lattice-Boltzmann study

Jia-tuo An[1], *Da-fan Du[1], ***Li-jun Zhang[2], **An-ping Dong[1], and Bao-de Sun[1]

1. Shanghai Key Lab of Advanced High-temperature Materials and Precision Forming and State Key Lab of Metal Matrix Composites, School of Materials Science and Engineering, Shanghai Jiao Tong University, Shanghai 200240, China

2. State Key Laboratory of Powder Metallurgy, Central South University, Changsha 410083, China

Abstract: Thin-walled aluminum alloys, prized for their high specific strength, are critical to modern aerospace and other advanced industries. Counter-gravity casting (CGC) is a premier method for fabricating such components, where precise control over solidification microstructure is paramount. However, this control is challenged by the complex interplay of forced and natural convection during solidification. This study employs a coupled multiple-relaxation-time lattice Boltzmann (D2Q9) and quantitative phase-field model to simulate dendritic growth in a thin-walled Al-0.576wt.%Cu alloy. Simulations reveal that convection disrupts dendritic symmetry: for equiaxed crystals, solute plumes and asymmetric arm growth are observed, while for columnar dendrites, an optimal applied force exists that refines the microstructure without compromising economic viability. Furthermore, forced convection consistently reduces the inclination angle of primary dendrites. These findings, validated against experimental data, elucidate the micro-mechanisms of dendritic growth under convection, providing critical theoretical guidance for optimizing CGC processes.

Keywords: phase-field method; simulation; solidification; dendritic growth

CLC numbers: TG146.21 **Document code:** A **Article ID:** 1672-6421(2026)03-327-09

1 Introduction

As industries advance, the demand for lightweighting has been steadily increasing in various industry sectors, particularly within the aerospace industry. Accordingly, thin-walled structures have become widely used in multiple aerospace components, including aerospace engines[1]. However, traditional gravity casting (GC) techniques often lead to defects such as incomplete filling, inclusions, shrinkage porosity/cavities within thin-walled castings, resulting from uncontrollable natural convections[1]. These conventional methods face even greater difficulties in producing high-quality and complex-shaped thin-walled castings. In recent years, the emergence and development of counter-gravity casting (CGC) technology have proven its ability in manufacturing complex and thin-walled components[2]. Such technology has found widespread applications in various industry sectors, including aerospace[1], automotive manufacturing[3, 4], and electronics[5]. Nowadays, the primary categories of CGC techniques include low-pressure casting (LPC)[6], counter-pressure casting (CPC)[7], vacuum suction casting (VSC)[8], and adjusted pressure casting (APC)[9]. Unlike the GC process, the CGC process involves the molten metal being subjected to an artificially applied force in the direction opposite to gravity, in addition to the gravitational force. As a result, in the CGC process, the filling speed of the melt is more stable and controllable, resulting in higher-quality castings that are virtually

***Da-fan Du**

Ph. D., Associate Professor. His research primarily focuses on solidification process control and microstructure engineering.

E-mail: dafand@sjtu.edu.cn

****An-ping Dong**

E-mail: apdong@sjtu.edu.cn

*****Li-jun Zhang**

E-mail: lijun.zhang@csu.edu.cn

Received: 2025-08-29; Revised: 2025-11-24; Accepted: 2025-12-15

free of defects such as inclusions, oxides, shrinkage porosity, and cavities. However, the solidification micro-mechanisms of thin-walled alloys still require in-depth investigation, and a quantitative description of the solidification microstructure in this process is essential.

In fact, in the CGC process, the evolution of the solidification microstructure in thin-walled castings is rather complex, as different convection patterns are involved, including natural convection and forced convection. The applied force can lead to forced convection, which can alleviate or strengthen the effects of natural convection caused by gravity. Therefore, in the CGC process, quantitative investigation of the solidification microstructure evolution in thin-walled castings is rather challenging. For many years, the experimental methods have been the primary tools for analyzing the evolution of solidification microstructure in thin-walled CGC castings. Zhang et al.[10] investigated the impact of casting methods, including GC, LPC, and CPC, on the microstructure of ZM5 alloy. They observed finer and more uniform precipitated particles, as well as fewer casting defects, in the CPC samples. Yan et al.[11] found that increasing the solidification pressure could enhance extrusion and infiltration among the dendrites, resulting in a finer and denser solidification microstructure. Li et al.[12] conducted real-time X-ray observations of the solidification process of Al-20wt.%Cu alloy under gravity in thin-walled castings. They discovered that the filling and solidification behavior of the alloy melt primarily depended on the wall thickness. As the wall thickness decreased, the dendritic network became denser, and the melt filling time was reduced[12]. Simultaneously, dendrites nucleated on the colder mold wall and grew inward towards the center of the casting[12]. Due to the confined space within thin-walled castings, convection between growing dendrites and the melt becomes significant during the solidification process. Therefore, the process of dendritic growth involves complex interactions among the flow field, solute field, temperature field, and solid-liquid phase transformation. Quantitative study of the effects of individual parameters on solidification microstructure in thin-walled CGC castings through traditional experimental methods is challenging, especially for the dendritic growth under convection. Consequently, few studies have systematically investigated the microscopic mechanisms of dendritic growth under convection in thin-walled CGC castings. Therefore, employing numerical simulations to quantitatively investigate the effects of complex convection on the solidification microstructure is particularly crucial.

In recent years, with the refinement and development of the phase-field method (PFM)[13] and the lattice Boltzmann method (LBM)[14], an increasing number of researchers have adopted a coupled approach combining these two methods to simulate the process of dendritic growth[15, 16]. Miller et al.[17, 18] first proposed and adopted the combination of PFM and LBM to simulate the dendritic growth under convection. Then, Medvedev et al.[19] developed the phase-field lattice Boltzmann method (PF-LBM). Since then, an increasing number of researchers have been drawn to investigating solidification microstructure morphologies under convective conditions using PF-LBM. Zhang et al.[20] coupled the phase-field method with the LBM to simulate the morphological evolution of equiaxed grains and dendrites in an Al-4wt.%Cu alloy under both natural and forced convection. Their findings indicated that convection leads to the deflection of the primary dendritic trunk. Zhang et al.[21] simulated the directional solidification process of a CM247LC alloy using a coupled phase-field and LBM, finding that the crystal orientation angle exerted only a minor effect on the solute plume morphology. These studies have demonstrated the effectiveness of PFM and LBM in investigating solidification micro-mechanisms in castings, laying a solid foundation for future applications in practical casting processes. However, most of present research adopted single-relaxation-time (SRT) LBM, providing high computational efficiency with the sacrifice of numerical accuracy. Compared to SRT-LBM, the multiple-relaxation-time (MRT) LBM model exhibits a higher numerical accuracy[22, 23]. Thus, to quantitatively describe the effects of convection on the evolution of solidification microstructure, an MRT-LBM is necessary in the simulation process.

This work aims to investigate the effects of complex convection on solidification microstructures in thin-walled CGC castings. A lower solute concentration results in a larger capillary length, thereby reducing computational cost. Accordingly, an Al-0.576wt.%Cu alloy was used in this study. A PFM coupled with an MRT-LBM D2Q9 model was utilized to quantitatively simulate the dendritic growth during the solidification of the Al-0.576 wt.%Cu alloy in thin-walled casting conditions. The dendritic morphologies, concentration distribution, and convection velocity distribution around the dendrite tips under non-convection, natural convection, and forced convection conditions were investigated. Consequently, the effects of forced convection on dendritic growth in CGC were studied, offering practical guidance for CGC production.

2 Numerical methods

2.1 Phase-field model

The quantitative phase-field model for binary alloy proposed by Echebarria et al.[24] was employed to simulate the evolution of phase-field ϕ and dimensionless supersaturation field U. In this model, ϕ=+1 represents solid phase, and ϕ=−1 represents liquid phase. U is the dimensionless solute concentration, which is expressed as[24]:

$$U=\frac{1}{1-k}\left(\frac{2c/c_{\infty}}{1+k-(1-k)g(\phi)}-1\right) \tag{1}$$

where c represents the solute concentration, c_{∞} is the nominal composition of the alloy, k is the partition coefficient, $g(\phi)=\phi$ is the interpolation function[24].

The governing equations of ϕ and U under convection can

be expressed as below[20, 24]:

$$\tau(\boldsymbol{n})^2\frac{\partial\phi}{\partial t}=\nabla\cdot\left[a_{\mathrm{s}}(\boldsymbol{n})^2\nabla\phi\right]+\partial_x\left(|\nabla\phi|^2\,a_{\mathrm{s}}(\boldsymbol{n})\frac{\partial a_{\mathrm{s}}(\boldsymbol{n})}{\partial\left(\partial_x\phi\right)}\right)+\partial_y\left(|\nabla\phi|^2\,a_{\mathrm{s}}(\boldsymbol{n})\frac{\partial a_{\mathrm{s}}(\boldsymbol{n})}{\partial\left(\partial_y\phi\right)}\right)+\phi-\phi^3-\lambda\left(1-\phi^2\right)^2\left(U+\theta\right) \tag{2}$$

$$\left(\frac{1+k}{2}-\frac{1-k}{2}\phi\right)\frac{\partial U}{\partial t}=\nabla\cdot\left(\tilde{D}q(\phi)\nabla U+a(\phi)\left(1+(1-k)U\right)\frac{\partial\phi}{\partial t}\frac{\nabla\phi}{|\nabla\phi|}\right)+\frac{1}{2}\left[1+\left(1-k\right)U\right]\frac{\partial\phi}{\partial t}-\frac{1}{2}f_1\tilde{\boldsymbol{v}}_{\mathrm{p}}\cdot\left\{\left[1+k-\left(1-k\right)\phi\right]\nabla U-\left[1+\left(1-k\right)U\right]\nabla\phi\right\} \tag{3}$$

where $\tau(\boldsymbol{n})$ is the relaxation time. For isothermal solidification, $\tau\left(\boldsymbol{n}\right)=\left[Mc_\infty\left(1+\left(1-k\right)U\right)\right]a_{\mathrm{s}}(\boldsymbol{n})^2$, depending on solutal diffusion[25]. $M=\left|m\right|\left(1-k\right)/\Delta T_0$ is the dimensionless liquidus slope, and m is the liquidus slope[25]. $\Delta T_0=\left|m\right|c_1^0\left(1-k\right)$ is the equilibrium solidification temperature range[25]. c_1^0 is the equilibrium liquid composition at initial temperature T_0. $a_{\mathrm{s}}(\boldsymbol{n})=1-3\varepsilon_4+4\varepsilon_4\left(\phi_x^4+\phi_y^4\right)/\left(\phi_x^2+\phi_y^2\right)^2$ is the anisotropy function, ϕ_x and ϕ_y are the partial derivatives of ϕ in the X-direction and Y-direction respectively, which are the components of the unit vector $\boldsymbol{n}=-\nabla\phi/\left|\nabla\phi\right|$ normal to the interface. ε_4 is the anisotropic strength, $\lambda=\mathrm{a}_1W_0/d_0$ is the coupling factor[24], a_1=0.8839 is a constant[26], and W_0 is the solid-liquid interface width. $d_0=\Gamma/\Delta T_0$ is the chemical capillary length[24], Γ is the Gibbs-Thomson coefficient, $\theta=(T-T_0)/\Delta T_0$ is the equivalent dimensionless undercooling[27], and T is the temperature at a fixed point and time. For directional solidification, $\tau\left(\boldsymbol{n}\right)=\left[1-\left(1-k\right)\left(G_x\cdot x-R\cdot t\right)/\Delta T_0\right]a_{\mathrm{s}}(\boldsymbol{n})^2$, depending on temperature[24]. G_x is the temperature gradient along X-direction, and x is the distance from the nucleation site. $\tilde{D}=\mathrm{a}_2\lambda$ is the dimensionless solutal diffusion coefficient in liquid phase[24]. a_2=0.6267 is a constant[26]. $q(\phi)=\phi$ and $a(\phi)=\sqrt{2}/2$ are the interpolation functions[24]. $f_1=(1-\phi)/2$ is the liquid phase fraction. $\tilde{\boldsymbol{v}}_{\mathrm{p}}$ is the dimensionless melt velocity in this study, which can be expressed as:

$$\tilde{\boldsymbol{v}}_{\mathrm{p}}=\mathrm{a}_1\mathrm{a}_2\frac{\boldsymbol{v}d_0}{D}\left(\frac{W_0}{d_0}\right)^2 \tag{4}$$

where D is the solute diffusion coefficient in liquid phase, and $\boldsymbol{v}$ is the melt velocity.

For the directional solidification, the frozen temperature approximation was employed, which can be described as[27]:

$$T=T_0+G_xx-R\times t \tag{5}$$

where R is the cooling rate, t is the simulation time, and T_0 is the reference temperature at x=0 and t=0.

2.2 MRT-LBM D2Q9 model

To model the melt flow behavior and convection, the MRT-LBM D2Q9 model[28] was employed in this work. The governing equation of particle distribution function (PDF) can be described as[28]:

$$f_i\left(\boldsymbol{x}+\boldsymbol{e}_i\delta_x,t+\delta_t\right)=f_i\left(\boldsymbol{x},t\right)-\Omega_{ij}\left[f_j\left(\boldsymbol{x},t\right)-f_j^{\mathrm{eq}}\left(\boldsymbol{x},t\right)\right]+\delta_tF_i\left(\boldsymbol{x},t\right) \tag{6}$$

where $f_i(\boldsymbol{x},t)$ and $f_j(\boldsymbol{x},t)$ are the PDFs at position x and time t along the ith and jth direction, respectively. $f_j^{\mathrm{eq}}\left(\boldsymbol{x},t\right)$ denotes the equilibrium PDF at position x and time t along the jth direction in the lattice space. δ_x represents the spactial interval, and δ_t denotes the time step, and $\boldsymbol{e}_i$ is the unit discrete velocity associated with the ith lattice direction, which is expressed as[28]:

$$\boldsymbol{e}_i=\begin{cases}(0,0) & i=0\\ \left(\cos\left[(i-1)\pi/2\right],\sin\left[(i-1)\pi/2\right]\right) & i=1\text{–}4\\ \sqrt{2}\left(\cos\left[(2i-9)\pi/4\right],\sin\left[(2i-9)\pi/4\right]\right) & i=5\text{–}8\end{cases} \tag{7}$$

$\Omega=\boldsymbol{M}^{-1}\boldsymbol{S}\boldsymbol{M}$ is the collision matrix, and $\boldsymbol{M}$ is the transformation matrix between the lattice space and velocity space, which is defined as[28]:

$$\boldsymbol{M}=\begin{pmatrix}1&1&1&1&1&1&1&1&1\\-4&-1&-1&-1&-1&2&2&2&2\\4&-2&-2&-2&-2&1&1&1&1\\0&1&0&-1&0&1&-1&-1&1\\0&-2&0&2&0&1&-1&-1&1\\0&0&1&0&-1&1&1&-1&-1\\0&0&-2&0&2&1&1&-1&-1\\0&1&-1&1&-1&0&0&0&0\\0&0&0&0&0&1&-1&1&-1\end{pmatrix} \tag{8}$$

$\boldsymbol{S}$ is a diagonal matrix containing multi-relaxation times in 9×9 dimension, and can be defined as[29]:

$$\boldsymbol{S}=\mathrm{diag}\left(0,1.63,1.14,0,1.92,0,1.92,s_\upsilon,s_\upsilon\right) \tag{9}$$

where $s_\upsilon=0.5+1/\tau$ is the relaxation parameter[29]. $\tau=0.5+3\upsilon$ is relaxation time, and υ is the kinematic viscosity[29].

$f_i(\boldsymbol{x},t)$ is the external force term, which can be calculated by[30]

$$\boldsymbol{G}=\boldsymbol{M}^{-1}\left(\boldsymbol{I}-\frac{1}{2}\boldsymbol{S}\right)\boldsymbol{M}\bar{\boldsymbol{F}} \tag{10}$$

where $\boldsymbol{G}=\left(F_0,F_1,...,F_8\right)^T$, $\boldsymbol{I}$ is the unit matrix, and $\bar{\boldsymbol{F}}=\left(\bar{F}_0,\bar{F}_1,...,\bar{F}_8\right)^T$ with

$$\bar{F}_i=w_i\left[\frac{\boldsymbol{c}_i\cdot\boldsymbol{G}}{c_{\mathrm{s}}^2}+\frac{\boldsymbol{v}\boldsymbol{G}:\left(\boldsymbol{c}_i\boldsymbol{c}_i-c_{\mathrm{s}}^2\boldsymbol{I}\right)}{2c_{\mathrm{s}}^4}\right] \tag{11}$$

where w_i is the weight factor, which can be defined as[28]:

$$w_i=\begin{cases}4/9, & i=0\\ 1/9, & i=1\text{–}4\\ 1/36, & i=5\text{–}8\end{cases} \tag{12}$$

where c_i is the discrete velocity, $c_s^2=\delta_x^2/3\delta_t^2$ is the lattice sound speed. $\boldsymbol{G}=G_x\vec{i}+G_y\vec{j}$ represents the resultant external force, including the buoyancy force $G_B(\boldsymbol{x},t)$, dissipative drag force $G_D(\boldsymbol{x},t)$ and applied force $G_F(\boldsymbol{x},t)$, which can be calculated by[25, 31, 32]

$$G(\boldsymbol{x},t)=G_B(\boldsymbol{x},t)+G_D(\boldsymbol{x},t)+G_F(\boldsymbol{x},t) \quad (13)$$

$$G_B(\boldsymbol{x},t)=-\rho\boldsymbol{g}\beta_c\left(c-c_l^0\right)f_l \quad (14)$$

$$G_D(\boldsymbol{x},t)=-\frac{2\rho\upsilon h}{W_0^2}f_l\left(1-f_l\right)^2\boldsymbol{v} \quad (15)$$

$$G_F(\boldsymbol{x},t)=-A\rho f_l\boldsymbol{e} \quad (16)$$

where $\rho=\sum_i f_i(\boldsymbol{x},t)$[28] denotes the fluid density in lattice space, $f_l=(1-\phi)/2$ is the fraction of liquid phase, β_c is the solute expansion coefficient, and $\boldsymbol{g}$=–9.8 m·s^{-2} is gravitational acceleration. The negative sign indicates the negative direction of Y-axis, h=2.757 is a constant[29], $\boldsymbol{v}$ is the macroscopic fluid velocity, and $A=P_y$ is the acceleration transformed by the external pressure gradient dp/dy in this study, and can be calculated by

$$P_y=\frac{\mathrm{d}p}{\rho\cdot\mathrm{d}y} \quad (17)$$

2.3 Simulation condition

To simulate dendritic growth in a space approaching the actual dimensions of thin-walled castings, an Al-0.576wt.%Cu alloy was selected as the model alloy due to its larger chemical capillary length[27]. Its physical properties and simulation-related parameters are presented in Table 1. The time step was set to be $\Delta t=0.8(\Delta x)^2/(4\tilde{D})$[33]. The initial concentration field was set by the dimensionless supersaturation, $\Omega_0=\left(c_l^0-c\right)/\left(c_l^0(1-k)\right)$=0.5[24], where c_l^0 denotes the initial concentration of liquid phase at the solid-liquid phase interface.

The boundary conditions for all simulations are illustrated in Fig. 1. For the phase-field and concentration field, periodic boundary conditions were applied at the top and bottom boundaries. The left boundary was assigned a zero-flux boundary condition, while the right boundary was treated as a symmetric boundary condition. For the flow field, periodic boundary conditions were also applied at the top and bottom boundaries. The left boundary employed a non-equilibrium extrapolation scheme for non-slip boundary conditions. The right boundary was set as symmetric, while the solid-liquid interfaces at the dendrite surfaces were treated with non-slip boundary conditions using a bounce-back scheme.

Table 1: Physical properties of Al-0.576wt.%Cu[20, 27, 34]

Parameter	Symbol	Value
Nominal concentration (wt.%)	c_∞	0.576
Liquidus slope (K·wt.%$^{-1}$)	m	–2.7
Equilibrium solute partition coefficient	k	0.14
Solute diffusion coefficient in liquid (m^2·s^{-1})	D	3×10^{-9}
Solute expansion coefficient (wt.%$^{-1}$)	β_c	–0.73
Gibbs-Thomson coefficient (K·m)	Γ	2.4×10^{-7}
Kinematic viscosity (m^2·s^{-1})	u	4.851×10^{-7}
Interface width (m)	W_0	9.375×10^{-7}
Gravitational acceleration (m·s^{-2})	g_0	–9.8
Cooling speed (K·s^{-1})	R	1
Temperature gradient (K·m^{-1})	G	2000
Transformed acceleration (m·s^{-2})	P_y	0.01
Anisotropic strength	ε_4	0.02
Space interval (W_0)	Δx	0.8
Time interval (s)	Δt	3.75×10^{-5}

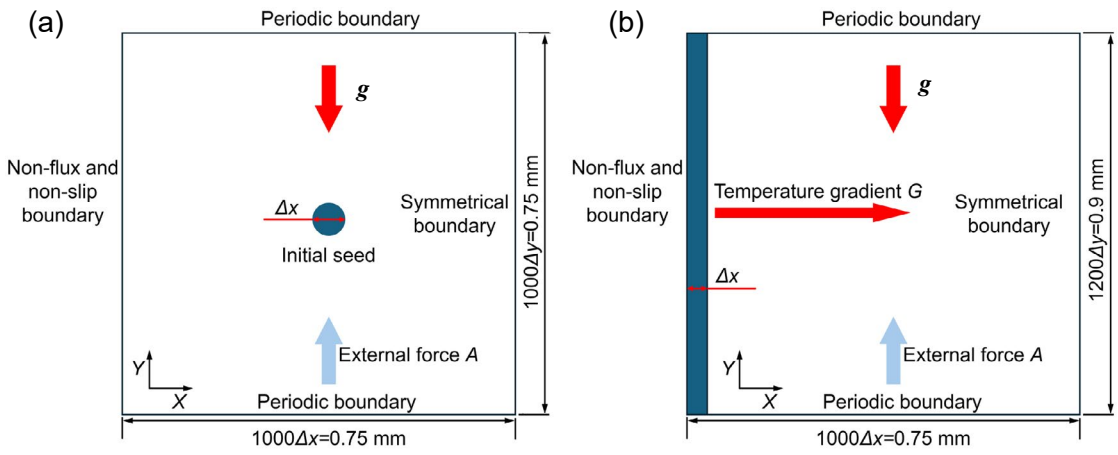

Fig. 1: Simulation conditions for equiaxed (a) and directionally solidified columnar (b) dendrites in a thin-walled Al-0.576wt.%Cu alloy

In this work, for isothermal solidification of equiaxed dendrites, the simulation domain was set to 1,000Δx×1,000Δy (with Δy=Δx)=0.75×0.75 mm^2. For directional solidification of dendrites, the simulation domain was set to 1,000Δx×1,200Δy (with Δy=Δx)=0.75×0.9 mm^2. A hybrid programming approach was employed utilizing Python and Taichi language to leverage graphics processing unit (GPU) acceleration for simulations. All simulations were conducted on a single NVIDIA Tesla V100-SXM2 GPU.

3 Results and discussion

3.1 Effects of convection patterns on equiaxed dendritic morphologies

Figure 2 shows the evolution of equiaxed dendritic solidification morphologies under three distinct flow conditions: non-convection, pure natural convection (P_y=0, g=9.8 m·s^{-2} or g=−9.8 m·s^{-2}), and forced convection (P_y=0.01 m·s^{-2}, g=−9.8 m·s^{-2}). Under non-convection conditions [Figs. 2(a1) and (a2)], the lengths of four primary dendritic trunks are comparable. However, in the presence of natural convection [Figs. 2(b1) and (b2)], the convective flow moves from the top to the bottom of the dendrite. As a result, upstream dendrites grow faster than their downstream counterparts, and secondary arms preferentially develop along the upstream sides of the primary dendrite trunks. The growth of downstream dendrites is suppressed and exhibits a splitting phenomenon, resulting from an accumulation of solute. For β_c<0, the rejected solute accumulates at the downstream side under gravity, leading to a solute plume phenomenon [Fig. 2(b1)], which is closely related to the formation of freckles in GC castings[35]. Under a gravitational acceleration of g=−g_0 [Figs. 2(c1) and (c2)], the solute plume appears on the upper side of the dendrite due to buoyancy-driven convection. Although the location of the solute plume changed, it still appears around the downstream dendrite tip. When the P_y=0.01 m·s^{-2} is implemented [Figs. 2(d1) and (d2)], at the 1×10^{4}th timestep, the length of downstream primary dendrite is longer than its upstream primary dendrite, indicating that the flow direction reversed at an earlier stage of solidification. The influence of gravity-driven

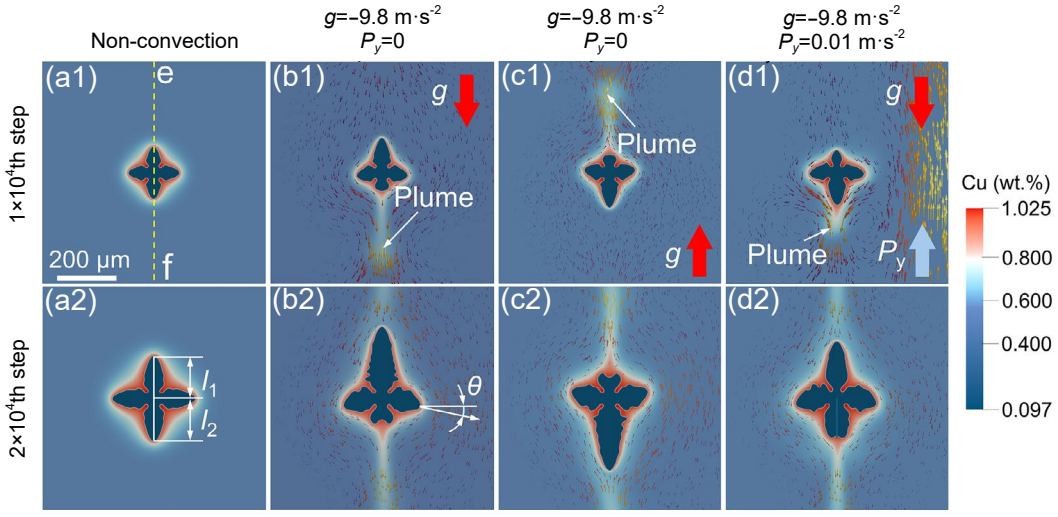

Fig. 2: Simulation results of equiaxed dendrites growth under different convection patterns: (a1)–(a2) non-convection; (b1)–(b2) g=g_0 and P_y=0; (c1)–(c2) g=−g_0 and P_y=0; (d1)–(d2) g=−g_0 and P_y=0.01 m·s^{-2}, at different simulation time: (a1)–(d1) t=0.375 s; (a2)–(d2) t=0.75 s

natural convection is reduced, causing the solute plume to remain more centralized and align closely with the dendrite tip. Therefore, in CGC, with the implementation of an appropriate applied force, the solute plume can be controlled or even eliminated, which can reduce the freckle defects in the solidification microstructure.

To further study the relationship between dendrite morphologies and convection, the concentration along the Line e-f [Fig. 2(a1)] was investigated and shown in Fig. 3. The maximum concentration value around the upstream dendrite tip is 0.954wt.% under natural convection, and 0.942wt.% (P_y=0.01 m·s^{-2}) under forced convection, which are larger than the 0.878wt.% without convection. Meanwhile, the maximum concentration around the downstream dendrite tip under forced convection is 0.834wt.%, which is higher than the 0.810wt.% under pure natural convection. The high solute concentration around dendrite tips decreases the local melting point, leading to a decrease in local undercooling[25]. Therefore, the growth velocity of dendrite tips decreases. Consequently, the downstream dendrite trunk can be shorter than that of the upstream dendrite trunk, and the horizontal primary dendrite trunks exhibit noticeable deflection [Fig. 2(b2)][20]. The deflection angle θ was measured by ImageJ. Under natural convection, the θ is 17.556°, whereas it decreases to 15.48° under forced convection. The deflection angle decreases by 2.076°, resulted by the decrease in convection strength around the dendrite. An asymmetry degree δ was used to quantitatively analyze the length difference between the upstream primary dendrite trunk and the downstream primary dendrite trunk. It is defined as:

$$\delta = \frac{|l_1 - l_2|}{l_1 + l_2} \tag{21}$$

where l_1 and l_2 are the lengths of the upstream primary dendrite trunk and downstream primary dendrite trunk, respectively [Fig. 2(a2)]. At the 2×10^{4}th timestep, under no convection, δ=0, while δ=0.52 under pure natural convection, and δ=0.17 under forced convection. Therefore, within the applied force in CGC, compared to GC with pure natural convection, the dendrite morphologies can be more symmetrical, making the solidification microstructure more uniform. This finding is in agreement with the experimental work of Chak et al.[36], indicating that the solidification microstructure is more uniform and there are fewer casting defects in the CGC cast aluminum alloy sample.

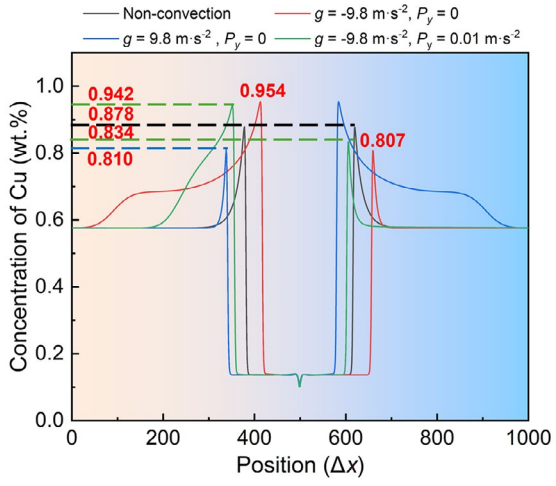

Fig. 3: Concentration distribution of solute Cu along Line e-f under different convection patterns

3.2 Effects of convection patterns on directionally solidified columnar dendritic morphologies

In thin-walled casting molds, nucleation typically initiates at the colder side mold walls, followed by dendritic growth progresses inward toward the central region of the casting[12]. Figure 4 illustrates the simulated results of directional solidification of dendrites. Under convection, the growth direction of the dendrites becomes inclined toward the direction of fluid flow. Under natural convection [Fig. 4(b)], the average deflection angle of the dendrites is 5.32°. Under forced convection [Figs. 4(c) and (d)], the average deflection angle of the dendrites is 4.45°, which decreases by 0.87°, resulting from the decrease in convection strength around the dendrite tips. However, when P_y increases again [Figs. 4(e) to (h)], the deflection angle changes little. Interestingly, there is a transformation of convection patterns. As shown in Fig. 4(c), at the 4×10^{4}th timestep, natural convection induced by gravity dominates near the dendrite tips, resulting in a fluid velocity primarily oriented along the negative *Y*-direction. However, in the region farther from the dendrites, where solute enrichment is relatively weak, the convection is mainly driven by the forced convection caused by the applied force. At the 6×10^{4}th timestep, natural convection becomes dominant throughout the thin-walled domain, causing the melt to flow predominantly along the negative *Y*-direction. As shown in Figs. 4(e) to (h), when the external force increases gradually, the strength of the forced convection far away from the dendrite tips also increases.

As shown in Figs. 4(b) and (d), under forced convection, the development of secondary dendrites is suppressed, and the competition between primary and secondary dendrites is alleviated [the yellow dashed circles in Figs. 4(b) and (d)]. As a result, the primary dendrites gain a growth advantage. Consequently, the solidification microstructure is finer than that under natural convection. As shown in Fig. 5, without convection, the primary dendrite arm spacing (PDAS) of this alloy is the largest, which is 86.67±22.38 μm. When P_y increases from 0 to 0.03 m·s^{-2}, the average PDAS decreases from 71.38 μm to 55.98 μm, indicating a finer solidification microstructure. Meanwhile, with the increase of P_y, the decrease of average PDAS slows down. As a conclusion, the implementation of applied force in CGC can lead to a finer solidification microstructure, agreeing with the experimental work of Zhang et al[10].

By analyzing the melt velocity along the m-n line [Fig. 4(a)], the convection behavior ahead of the dendrite tips can be evaluated. As illustrated in Fig. 6, when P_y=0.01 m·s^{-2}, as dendrites grow, the fluid velocity in the distal region eventually becomes fully aligned with the negative *Y*-direction, indicating that

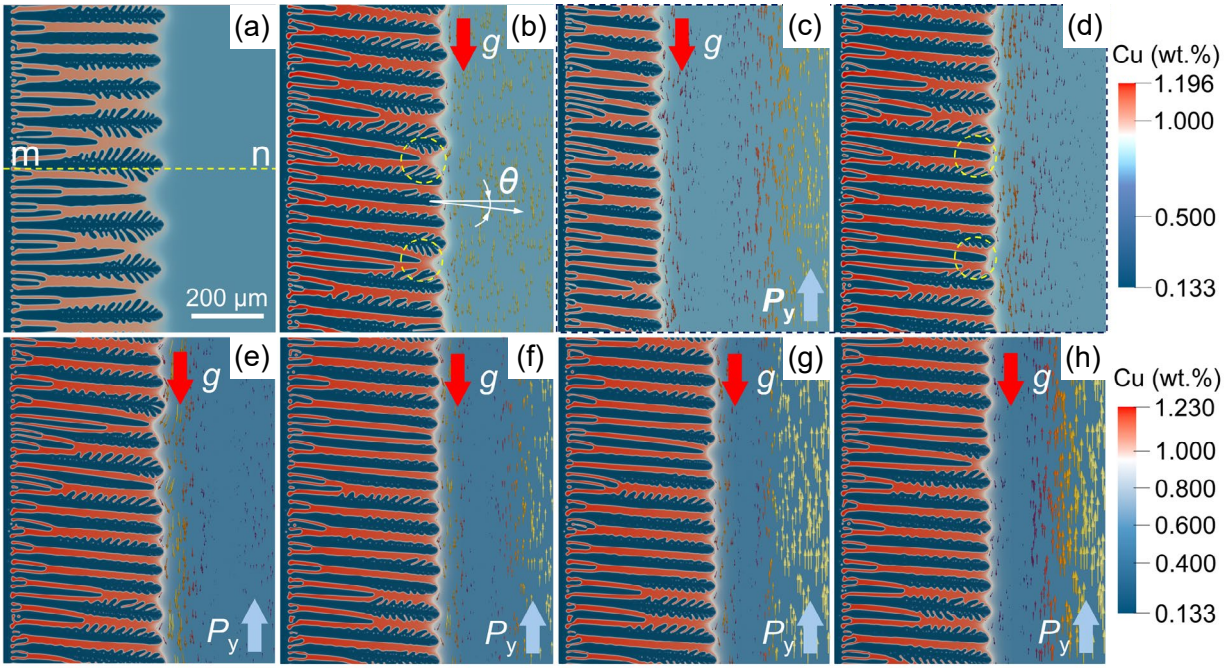

Fig. 4: Simulation results of directionally solidified columnar dendrites under different convection patterns: (a) non-convection (at the 6×10^{4}th timestep); (b) g=g_0 and P_y=0 (at the 6×10^{4}th timestep); (c) g=g_0 and P_y=0.01 m·s^{-2} (at the 4×10^{4}th timestep); (d) g=g_0 and P_y=0.01 m·s^{-2} (at the 6×10^{4}th timestep); (e) g=g_0 and P_y=0.015 m·s^{-2} (at the 6×10^{4}th timestep); (f) g=g_0 and P_y=0.02 m·s^{-2} (at the 6×10^{4}th timestep); (g) g=g_0 and P_y=0.025 m·s^{-2} (at the 6×10^{4}th timestep); (h) g=g_0 and P_y=0.03 m·s^{-2} (at the 6×10^{4}th timestep)

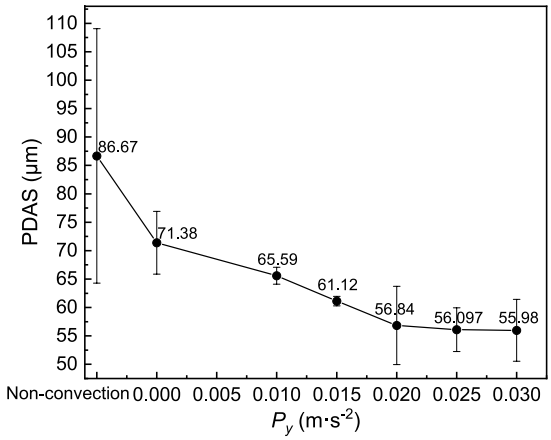

Fig. 5: Variation of PDAS under different convection patterns

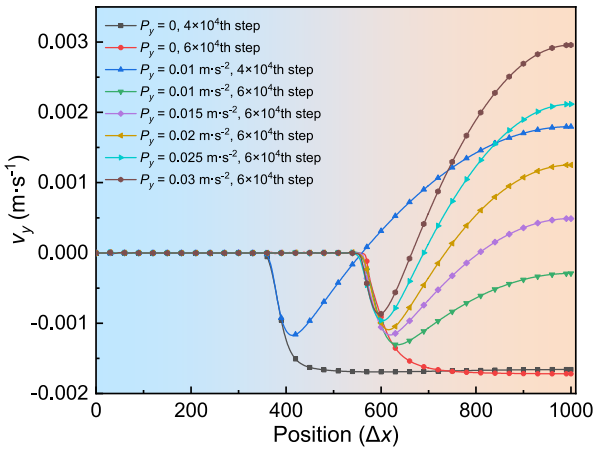

Fig. 6: Vertical velocity distribution along Line m-n under different convection patterns

gravity-driven natural convection has become the dominant flow mechanism. With the increase of P_y, the melt velocity in the distal region increases, and the melt flows along the positive Y-direction, indicating a strengthening of forced convection. Around the dendrite tips, as shown in Fig. 7, when P_y increases from 0 m·s^{-2} to 0.03 m·s^{-2}, the maximum vertical velocity decreases from –1.69×10^{-3} m·s^{-1} to –8.7×10^{-4} m·s^{-1} (negative sign means v_y is along the negative direction), indicating the decrease of convection strength. Therefore, in CGC, the applied force can lead to the decrease of convection strength induced by gravity, resulting in a finer solidification microstructure.

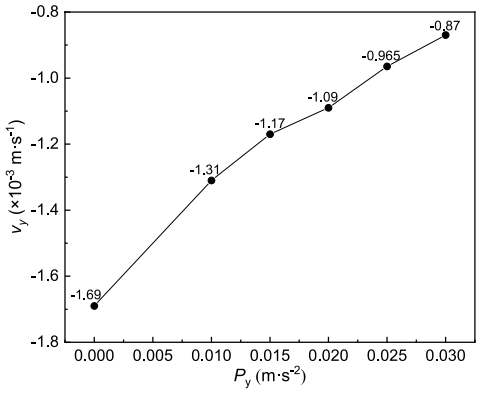

Fig. 7: Maximum vertical velocities around dendrite tips under different P_y at the 6×10^{4}th timestep

4 Conclusions

This study coupled the multiple-relaxation-time Lattice-Boltzmann method with the binary Karma phase-field model to simulate the influence of different convection conditions

on the morphology of Al-0.576wt.%Cu equiaxed dendrites and directionally solidified columnar dendrites in thin-walled castings. The main conclusions are as follows:

(1) Equiaxed dendrites exhibit solute plume phenomena under gravity-driven natural convection, leading to significant differences in the development of upstream and downstream dendrite arms. When a transformed acceleration of P_y=0.01 m·s^{-2} is implemented, the intensity of gravity-induced convection is reduced. The distance between the solute plume center and the dendrite tip decreases, and the tilt angle of the horizontal primary dendrite arms reduces from 17.556° to 15.48°, indicating that the freckle defects can be reduced and the solidification microstructure can be more uniform in CGC.

(2) Under a temperature gradient of G=2,000 K·m^{-1} and a cooling rate of R=1 K·s^{-1}, melt convection induces deflection of directionally solidified columnar dendrites in the thin-walled casting in the direction of fluid motion. The deflection angle decreases with a reduction in the convection intensity induced by gravity. The convection patterns can be different in spatial distribution, the convection pattern near the dendrite tips in the thin-walled space is predominantly governed by gravity-induced natural convection, whereas forced convection induced by P_y dominated at the far field region. As dendrites grow within the thin-walled cavity, the overall convection pattern evolves to become dominated by natural convection. With the increase of external force, the decrease in convection strength around dendrite tips lead to a reduction in average PDAS, indicating a finer solidification microstructure in counter-gravity casting. However, when P_y exceeds 0.02 m·s^{-2}, the fluctuation of average PDAS is small. Generally, the greater the applied force, the higher the production cost. Therefore, in practical production, there is an optimal applied force that balances the refinement of the solidification microstructure and the production cost.

(3) By simulating the growth morphology of equiaxed dendrites and directionally solidified columnar dendrites under various convection patterns in thin-walled castings, this research further elucidates the microscopic solidification mechanisms in both gravity casting and counter-gravity casting of thin-walled castings. This work provides valuable theoretical guidance for actual production practices.

Acknowledgments

This work was financially supported by the Advanced Materials-National Science and Technology Major Project (No. 2024ZD0600400), the Aeronautical Science Fund of China (No. 2023Z053057003), and the Science and Technology Commission of Shanghai Municipality, China (No. 23ZR1428800).

Conflict of interest

The authors declare that they have no known competing financial interests or personal relationships that could have appeared to influence the work reported in this paper.

References

[1] Yu Z W, Li F G, Zhang J, et al. Progess of the counter gravity casting technology in the superalloy large complicated thin-walled castings. Journal of Special Casting & Nonferrous Alloys, 2012, 32(12): 1103–1106. (In Chinese)
[2] Feng Z J, Li Y F, Wang W, et al. Counter-gravity casting. Foundry Equipment and Technology, 2019, 40(4): 71–76. (In Chinese)
[3] Huang J M, Zhao H D, Chen Z M. Microstructure and properties of A356 alloy wheels fabricated by low-pressure die casting with local squeeze. Journal of Materials Engineering and Performance, 2019, 28(4): 2137–2146.
[4] Dong G, Li S, Ma S, et al. Process optimization of A356 aluminum alloy wheel hub fabricated by low-pressure die casting with simulation and experimental coupling methods. Journal of Materials Research and Technology, 2023, 24: 3118–3132.
[5] Lehmhus D, Cen M, Struss A, et al. Thick film sensor manufacturing techniques for realization of smart components via low pressure die casting. Journal of Physics: Conference Series, 2024, 2692: 012007.
[6] Huang X, Xue X, Wang M, et al. Hot tearing behavior of ZL205A alloy cylindrical low-pressure castings with slit gating and feeding system. International Journal of Metalcasting, 2023, 17(4): 2970–2980.
[7] Jarfors A E W. Pressure different casting. In: Encyclopedia of Materials: Metals and alloys, Elsevier, 2022: 117–128.
[8] Liu S G, Cao F Y, Yi J Y, et al. Effect of depressurizing speed on mold filling behavior and entrainment of oxide film in vacuum suction casting of A356 alloy. Transactions of Nonferrous Metals Society of China, 2016, 26(12): 3292–3298.
[9] Dong A P, Du D F, Xing H, et al. Advanced adjusted pressure casting process. In: Proc. Precision Forming Technology of Large Superalloy Castings for Aircraft Engines, Singapore, Springer Singapore, 2021: 355–406.
[10] Zhang X L, Yu G K, Zou W B, et al. Effect of casting methods on microstructure and mechanical properties of ZM5 space flight magnesium alloy. China Foundry, 2018, 15(6): 418–421.
[11] Yan Q S, Yu H, Xu Z F, et al. Effect of holding pressure on the microstructure of vacuum counter-pressure casting aluminum alloy. Journal of Alloys and Compounds, 2010, 501(2): 352–357.
[12] Li F, Zhang J, Bian F, et al. Mechanism of filling and feeding of thin-walled structures during gravity casting. Materials, 2015, 8(6): 3701–3713.
[13] Tang Y, Zhang A, Liu H, et al. Insight into scale selection of dimensionless phase-field model of alloy solidification. Materials & Design, 2025, 254: 114028.
[14] Qin S, Hou G, Yang L, et al. One-step simplified lattice Boltzmann method of thermal flows under the Boussinesq approximation. Physical Review: E, 2023, 108(4): 045305. http://doi.org/10.1103/PhysRevE.108.045305.
[15] Sun D K, Zhu M, Pan S, et al. Lattice Boltzmann modeling of dendritic growth in a forced melt convection. Acta Materialia, 2009, 57(6): 1755–1767.
[16] Zhang A, Du J, Guo Z, et al. Lamellar eutectic growth under forced convection: A phase-field lattice-Boltzmann study based on a modified Jackson-Hunt theory. Physical Review: E, 2018, 98(4): 043301.
[17] Miller W, Succi S, Mansutti D. Lattice Boltzmann model for anisotropic liquid-solid phase transition. Physical Review Letter, 2001, 86(16): 3578–3581.
[18] Miller W, Succi S. A lattice Boltzmann model for anisotropic crystal growth from melt. Journal of Statistical Physics, 2002, 107(1): 173–186.
[19] Medvedev D, Kassner K. Lattice Boltzmann scheme for crystal growth in external flows. Physical Review: E, 2005, 72(5): 056703.

[20] Zhang A, Meng S, Guo Z, et al. Dendritic growth under natural and forced convection in Al-Cu alloys: From equiaxed to columnar dendrites and from 2D to 3D phase-field simulations. Metallurgical and Materials Transactions: B, 2019, 50(3): 1514–1526.
[21] Zhang Y J, Zhou J X, Yin Y J, et al. Numerical simulation of dendrite growth and solute convection during directional solidification of superalloy. Journal of Netshape Forming Engineering, 2023, 15(10): 13–20.
[22] Sun D K, Xing H, Dong X, et al. An anisotropic lattice Boltzmann-Phase field scheme for numerical simulations of dendritic growth with melt convection. International Journal of Heat and Mass Transfer, 2019, 133: 1240–1250.
[23] Luo L S, Liao W, Chen X, et al. Numerics of the lattice Boltzmann method: Effects of collision models on the lattice Boltzmann simulations. Physical Review: E, 2011, 83(5): 056710.
[24] Echebarria B, Folch R, Karma A, et al. Quantitative phase-field model of alloy solidification. Physical Review: E, 2004, 70: 061604. https://doi.org/10.1103/PhysRevE.70.061604
[25] Zhang A, Du J, Guo Z, et al. A phase-field lattice-boltzmann study on dendritic growth of Al-Cu alloy under convection. Metallurgical and Materials Transactions: B, 2018, 49(6): 3603–3615.
[26] Karma A. Phase-field formulation for quantitative modeling of alloy solidification. Physical Review Letter, 2001, 87(11): 115701.
[27] Takaki T, Ohno M, Shimokawabe T, et al. Two-dimensional phase-field simulations of dendrite competitive growth during the directional solidification of a binary alloy bicrystal. Acta Materialia, 2014, 81: 272–283.
[28] Wu J, Sun D, Chen W, et al. A unified lattice Boltzmann-phase field scheme for simulations of solutal dendrite growth in the presence of melt convection. International Journal of Heat and Mass Transfer, 2024, 220: 124958.
[29] Lallemand P, Luo L S. Theory of the lattice Boltzmann method: Dispersion, dissipation, isotropy, galilean invariance, and stability. Physical Review: E, 2000, 61: 6546–6562.
[30] Guo Z, Zheng C. Analysis of lattice Boltzmann equation for microscale gas flows: Relaxation times, boundary conditions and the Knudsen layer. International Journal of Computational Fluid Dynamics, 2008, 22(7): 465–473.
[31] Yang C, Xu Q, Liu B. Study of dendrite growth with natural convection in superalloy directional solidification via a multiphase-field-lattice Boltzmann model. Computational Materials Science, 2019, 158: 130–139.
[32] Zhang Y, Zhou J, Yin Y, et al. Study on the solutal convection during dendrite growth of superalloy under directional solidification condition. Journal of Materials Research and Technology, 2023, 23: 3916–3927.
[33] Tourret D, Karma A. Growth competition of columnar dendritic grains: A phase-field study. Acta Materialia, 2015, 82: 64–83.
[34] Boukellal A K, Rouby M, Debierre J M. Tip dynamics for equiaxed Al-Cu dendrites in thin samples: Phase-field study of thermodynamic effects. Computational Materials Science, 2021, 186: 110051.
[35] Ren N, Li J, Panwisawas C, et al. Insight into the sensitivities of freckles in the directional solidification of single-crystal turbine blades. Journal of Manufacturing Processes, 2022, 77: 219–28.
[36] Chak V, Chattopadhyay H, Alam M M. Investigating the effect of counter gravity mold filling on microstructure and mechanical properties of cast aluminium. International Journal of Mathematical, Engineering and Management Sciences, 2020, 5(3): 497–506.